Anisotropic stress correlations in two-dimensional liquids

Bin Wu, Takuya Iwashita, and Takeshi Egami

Phys. Rev. E **91**, 032301 — Published 2 March 2015

DOI: 10.1103/PhysRevE.91.032301

ANISOTROPIC STRESS CORRELATIONS IN 2D LIQUIDS

Bin Wu[1], Takuya Iwashita[2], Takeshi Egami[1,2,3,*]

1, Department of Physics and Astronomy, Joint Institute of Neutron Science, University of Tennessee, Knoxville, Tennessee 37996, USA

2, Department of Materials Science and Engineering, University of Tennessee, Knoxville, Tennessee 37996, USA

3, Oak Ridge National Laboratory, Oak Ridge, Tennessee 37831, USA

* To whom correspondence should be addressed: egami@utk.edu

Abstract

In this paper we demonstrate the presence of anisotropic stress correlations in the simulated 2D liquids. Whereas the temporal correlation of macroscopic shear stress is known to contribute to viscosity via the Green-Kubo formula, the general question regarding angular dependence of the spatial correlation among atomic level stresses in liquids without external shear has not been explored. We observed the apparent anisotropicity with well-defined symmetry which can be explained in terms of the elastic continuum theory by Eshelby. In addition, we found that the shear stress correlation is screened compared to the prediction by the elastic continuum theory, and the screening length depends on temperature and follows the power law, suggesting divergence around the glass transition temperature. The success of the Eshelby theory to explain the anisotropy of the stress correlations justifies the idea that the mismatch between the atom and its nearest neighbor cage produces the atomic level stress as well as the long-range stress fields.

1. Introduction

A liquid shows time-dependent response to external shear stress, with the characteristic timescale of the Maxwell relaxation time, $\tau_M = \eta / G_\infty$, where η is viscosity and G_∞ is the high-frequency shear modulus [1]. If the timescale of experiment is longer than τ_M the liquid offers no resistance, but if it is shorter the liquid behaves like a solid with the elastic modulus similar to that of the crystalline solid made of the same chemical composition. Therefore a liquid can sustain an internal stress field for a timescale of τ_M. Indeed the viscosity is related to the temporal correlation of macroscopic shear stress through the Green-Kubo equation,

$$\eta = \frac{V}{kT} \int_0^\infty \langle \sigma^{xy}(0) \sigma^{xy}(t) \rangle dt, \tag{1}$$

where V is the sample volume, $\sigma^{xy}(t)$ is the shear stress in the x-y plane at time t, k is Boltzmann constant, and T is temperature [1]. The total shear stress in Eq. (1) can be broken into contributions from individual atoms thereby leading to the following expression [2, 3]:

$$\eta = \frac{1}{kTV} \int_0^\infty \langle \sum_{i,j} V_i \sigma_i^{xy}(0) V_j \sigma_j^{xy}(t) \rangle dt, \tag{2}$$

where V_i and σ_i^{xy} are the atomic volume and the atomic-level stress of the i-th atom. Hence the viscosity implicitly integrates spatiotemporal correlations of atomic level stresses. Levashov *et al.* [3] investigated the role of correlation length in the viscosity calculation and concluded that the viscosity is a nonlocal parameter. However the angular dependence of stress correlations was not explored in their study, where the correlation function was averaged spherically over relative distance between two particles, *i.e.* $|\vec{r_i} - \vec{r_j}|$.

In this article we study the anisotropy of spatial stress correlations in high temperature liquids. A simple two-dimensional (2D) colloidal liquid interacting with the screened Coulomb potential is simulated using classical molecular dynamics (MD) [4] for this purpose because the physics is the same for colloidal liquids as well as atomic liquids, and the anisotropy is more readily demonstrated in 2D. It is found that the computed correlation functions are distinctively anisotropic and characterized by well-defined two-fold or four-fold symmetries depending on the elements of the stress tensor. In order to identify the underlying mechanism of the observed anisotropy, we explain the simulation results in terms of Eshelby's theory of inclusion [5]. This theory was originally developed within the framework of continuum elasticity and solves the problem where a region ("inclusion") undergoes deformation constrained by its surroundings ("matrix"). For instance, when an elliptical subject is squeezed into a spherical hole, Eshelby's theory predicts a long-ranged and anisotropic elastic field outside the hole, *i.e.* in the matrix. Recently more studies have been reported on the applicability of Eshelby's theory in amorphous materials concerning their plasticity [6-25]. Different from previous reports that focused on supercooled liquids [6], glasses [7, 9-20, 22, 23] or colloids [24, 25] under external perturbation, *e.g.* shear, the present work extends the idea to high temperature liquids in equilibrium without an applied stress by using the concept of the atomic-level stresses.

The rest of this paper is organized as follows. In Sec. II, we describe our MD simulation setup and data analysis methods used to identify the boundary of liquid phase and to calculate stress correlation functions. In Sec. III, we first demonstrate that the spatial stress correlation functions in two-dimensional (2D) liquids are distinctively anisotropic. Then we investigate the nature of their oscillations and temperature dependent amplitudes. In Sec. IV, we present the stress fields calculated using Eshelby's theory and compare their symmetries with those of the simulation results. We summarize conclusions in Sec. V.

2. Molecular dynamics simulation

A. Simulation setup

We used the LAMMPS [26] to carry out two-dimensional molecular dynamics simulations. The setup is similar to the one reported in Refs. [27, 28]. We consider a monoatomic system interacting through pairwise Yukawa potential [29]. The choice of this potential owes to its success in describing interaction between charged colloids, *e.g.* dendrimers [30]. Its mathematical expression is presented below:

$$V(r) = U_0 \frac{\sigma}{r} \exp\left(-\lambda \frac{r-\sigma}{\sigma}\right), \tag{3}$$

where U_0 defines the strength of the interaction, λ is the screening parameter, σ is the size of a particle, and r represents the inter-particle distance. With employment of reduced unit formalism, we kept $U_0 = 1$, $\sigma = 1$, Boltzmann constant $k = 1$, and the mass of a particle $m = 1$ throughout the simulations. Moreover, we set $\lambda = 8$ and the cutoff distance for force evaluation as 4.1. We used a rectangular simulation box and applied periodic boundary condition on both directions. The ratio of the lengths of two sides is $2{:}\sqrt{3}$ for the sake of minimizing box size effect [27, 28, 31]. All simulation runs were performed under canonical ensemble while the temperature control was achieved by Nose-Hoover thermostat. The number of particles $N = 2500$, the area of simulation box $A = 2173.91$, and therefore the number density $\rho = \frac{N}{A} = 1.15$. The time step for integrating equations of motion via Verlet algorithm is 0.005 in reduced unit. We used the triangular crystalline lattice as the initial structure and gradually heated the system to each of the interested temperatures. We waited 10^7 time steps after the targeted temperature was reached and then collected 10^4 frames of trajectories, which were 10^3 time steps apart. The Maxwell relaxation time deduced from temporal correlation of macroscopic shear stress ranges from 0.2985 to 0.0512 (approximately 60 and 10 MD steps respectively) at the studied temperatures of 1 to 7 in liquid phase. Hence one can realize that the system is truly in equilibrium before the data collection.

B. Phase behavior

We use the potential energy per atom, E_a, to qualitatively monitor the phase behavior of the system under study. This quantity can be computed via the following equation:

$$E_a = \langle \frac{1}{2N} \sum_i \sum_{j \neq i} V(r_{ij}) \rangle. \quad (4)$$

The results are presented in Fig. 1 as a function of the reduced temperature T^*. At low temperatures the system is expected to be stable in the crystalline phase where E_a increases linearly with T^*. As temperature approaches approximately 0.9, the system starts to melt, signified by the emergence of the steep slope. The system ultimately enters the liquid phase at temperature around 1.0, where E_a resumes linear dependence on T^*.

There has been an ongoing debate over the melting mechanism in two dimensions. On one hand, the Kosterlitz-Thouless-Halperin-Nelson-Young (KTHNY) theory [32-35] predicts that the system can experience a hexatic phase in its path of transformation from a crystal to a liquid. The signature of this hexatic phase is the quasi-long range orientational order. On the other hand, 2D melting is believed to be a simple first-order phase transition [36]. There have been extensive studies to support both sides. Since deciphering the melting process is not the primary interest of present study, we focus on identifying the boundary of liquid phase using the bond orientational order parameter.

Taking the x axis as the reference axis, the bond angle between the particle k and each of its nearest neighbors j can be defined. The angle θ_{kj} should satisfy $\cos(6\theta_{kj}) = 1$ condition in the perfect crystalline phase and gradually diverge from it statistically as temperature increases. Hence the local bond angular order is quantified by

$$\Psi_6(\vec{r}) = \frac{1}{N_k}\sum_{j=1}^{N_k} e^{i6\theta_{kj}}, \tag{5}$$

where N_k represents number of nearest neighbors of the particle k. Its autocorrelation function, which is defined by Eq. (6), provides a measure of the range of the orientational order.

$$g_6(r) = \langle \Psi_6^*(\vec{r})\Psi_6(0)\rangle. \tag{6}$$

Fig. 2 illustrates $g_6(r)$ at temperatures in the vicinity of the melting point. In the crystalline phase, $g_6(r)$ converges to a finite asymptotic value which indicates the presence of long range orientational order. A possible hexatic phase is found at $T^* = 0.95$, where $g_6(r)$ decays algebraically suggesting a quasi-long range order of bond orientation exists in the system. As soon as the particles form liquids, the asymptotic form of $g_6(r)$ changes to an exponential decay over r. Therefore, the system is indeed in the liquid phase at $T^* \geq 1$.

C. Atomic level stress tensor

We assess the stresses at each particle via the atomic level stress [2], which can be computed from,

$$\sigma_i^{\alpha\beta} = \frac{1}{2A_i}\sum_j \frac{1}{r_{ij}}\frac{dV(r_{ij})}{dr} r_{ij}^{\alpha} r_{ij}^{\beta}, \tag{7}$$

where α and β indicate the corresponding Cartesian component while the summation runs over all particles residing inside the circle centered at the particle i with the radius being the cutoff distance set for MD simulation. A_i is the atomic area that can be evaluated using the Voronoi polyhedra. However, for the sake of simplicity, this work replaces it with the average atomic area defined by $A_{ave} = \frac{A}{N}$, where A is the total area of the simulation box.

D. Spatial stress correlation functions

The spatial stress correlation functions are the most important quantities in the present study. The functions correlate one component or some combinations of the elements in the stress tensor of one particle with that/those of other's. We present the spatial *x-y* shear stress correlation function as one example, which takes the following expression:

$$C_{s1,s1}(\vec{r}) = \langle \frac{\sum_i \sum_{j \neq i} \sigma_i^{s1} \sigma_j^{s1} \delta(\vec{r} - \vec{r_i} + \vec{r_j})}{\sqrt{\sum_i \left(\sigma_i^{s1}\right)^2} \sqrt{\sum_j \left(\sigma_j^{s1}\right)^2}} \rangle, \tag{8}$$

where $\sigma^{s1} = \sigma^{xy}$. It is important to note that the angular dependence of this correlation function is preserved in contrast to $g_6(r)$. We will show below the elastic fields are characterized by 4θ or 2θ symmetries, where θ is the polar angle. In addition to the *x-y* shear stress, we also consider the hydrostatic pressure, $p = \left(\sigma^{xx} + \sigma^{yy}\right)/2$, as well as the other shear stress, $\sigma^{s2} = \left(\sigma^{xx} - \sigma^{yy}\right)/2$, for auto- and cross correlations. We note that the hydrostatic pressure of each particle is subtracted by its ensemble average value, which accounts for the external pressure applied to keep the volume of the system constant, in the correlation analysis.

3. Stress correlations in liquids

In this section, we illustrate the existence of anisotropic correlations among the atomic level stresses in the 2D Yukawa liquids. The correlation functions are characterized by well-defined 4θ or 2θ symmetry which resembles the stress pattern in the matrix induced by a circular inclusion to be introduced later. We then examine the nature of their oscillations and temperature dependent amplitudes.

A. Symmetry

In Fig. 3, we present the spatial autocorrelation of the x-y shear stress computed at temperature $T^* = 1$. In Fig. 3 (a) the scale of color scheme matches the maximum intensity of the correlation function. One clearly sees four bright spots near the center due to the nearest neighbors overshadowing the rest, each of which takes one corner of the diagonals. The four fold symmetry is evident. For clear visualization of the far field we rescaled the color scheme in Fig. 3 (b). The innermost set of four spots, which are well separated in panel (a), almost merge to form a circle except for the gaps along the x- and y-axis directions under the new scale. Immediately following the first set, one sees two sets of four segments with one bearing positive intensity following the diagonal direction and the other carrying negative magnitude following the $\cos(4\theta) = 1$ directions. Outside these two sets of four spots, the spots merge into a rounded square. As the distance from the center further increases the correlation function shows successive positive and negative oscillations in intensity, resulting in a pattern similar to the propagating waves. Moreover, the correlation in the diagonal directions is considerably stronger than that in the $\cos(4\theta) = 1$ directions.

To demonstrate that the unique pattern of spatial shear stress correlation function in the liquid phase is not an artifact resulting from anisotropic packing of particles, we present the 2D pair distribution function (PDF) before and after the melting in Fig. 4. Fig. 4 (a) serves as the benchmark, where the system obviously maintains a crystalline order. Each particle has exactly six nearest neighbors. In contrast, as shown in Fig. 4 (b) the 2D PDF is clearly isotropic in the liquid phase for which the previous stress correlation analysis is performed. This confirms that the spatial shear stress correlation function in the Yukawa liquids is characterized by the 4θ symmetry.

We also calculated the spatial correlation function between σ^{s1} of particle i and other stress components of particle j. In Fig. 5, we present the results for σ_j^{s1} (panel (a)), p_j (panel (b)), and σ_j^{s2} (panel (c)) in the position of σ_j^{s1} in Eq. (8). The color scheme is chosen in the same manner that highlights the far field. The oscillatory nature of the correlation function is obvious. In addition, each of them is characterized by well-defined symmetry which agrees with the symmetry of the corresponding stress field of Eshelby's inclusion model as we discuss below. We also show in Fig. 6 the spatial correlations between the hydrostatic pressure of one particle and the *x*-*y* shear stress (panel (a)), hydrostatic pressure (panel (b)), and σ^{s2} (panel (c)) of others in the simulated Yukawa liquids. Their symmetrical patterns are again comparable to those of the Eshelby fields.

B. Oscillations in the stress correlation function

Whereas the spatial stress correlations in the 2D liquids agree with the Eshelby fields in terms of symmetry as shown above, the oscillatory nature is absent in the Eshelby fields. It is obvious that this oscillatory nature originates from the particular discreteness of the liquid, while Eshelby's theory, on the other hand, is built within the framework of continuum mechanics. In order to elucidate this point, we compare the oscillations with the structural parameters of liquids.

Firstly we examine the spatial *x*-*y* shear stress autocorrelation function. Its oscillations are compared with the derivate of PDF. In the panel (a) of Fig. 7 we present the comparison along the x axis. Considering the weak correlation in this direction, $C_{s1,s1}(\vec{r})$ is integrated over a wide solid angle to obtain better statistics, *i.e.* $\int_{-20^{\circ}}^{20^{\circ}} C_{s1,s1}(\vec{r})rd\theta$. In panel (b), we illustrate the counterpart in the $y = x$ direction, namely $\int_{42^{\circ}}^{48^{\circ}} C_{s1,s1}(\vec{r})rd\theta$. For simplicity, the amplitudes of the highest peaks are normalized to unity and the sign is flipped accordingly to make comparisons straightforward. In general, two curves show minor quantitative discrepancy at small r region but agree better as r increases. In panel (a), two curves differ on the heights of peaks up to the third positive peak and become almost identical beyond the distance of 4. In panel (b), the agreement at short r distance is worse, but gradually improves with increasing r.

The interpretations of the origin of the oscillations in the rest of the presented stress correlation functions are more straightforward. They are found to synchronize with the pair correlation function [1], $h(r) = g(r) - 1$, which describes the correlation of density fluctuations in the liquids. We show the comparisons in Fig. 8, where the respective correlation function is presented along the direction showing maximum intensity. Specifically the panel (a) illustrates $C_{p,p}(\mathrm{r})$, the panel (b) $C_{p,s1}(\mathrm{r})$, the panel (c) $C_{p,s2}(\mathrm{r})$, and the panel (d) $C_{s1,s2}(\mathrm{r})$. It is worthy of mentioning that $C_{p,s1}(\mathrm{r})$ is identical to $C_{s1,p}(\mathrm{r})$ owing to the equivalency of two components in the correlation analysis. Hence only the former is included in Fig. 8 to avoid redundancy. The correlation functions are rescaled so that they carry the same magnitude as that of the pair correlation function at the third peak position of the latter. The agreements are again generally excellent at distance beyond the second minimum in panels (a), (b), and (c). Whereas two curves in the panel (d) exhibit great similarity in terms of peaks' shape, they show minor misalignment.

C. Screening length

We now examine the amplitude of the anisotropic component of the *x*-*y* shear stress correlation and its temperature dependence. Because $C_{s1,s1}(\vec{r})$ is characterized by a strong $\cos(4\theta)$ component, we define the four-fold correlation function,

$$A_{4c}(r) = \frac{\int C_{s1,s1}(\vec{r})\cos(4\theta)d\theta}{g(r)}. \tag{9}$$

This function, shown in Fig. 9 (a), is characterized by oscillations. To examine the amplitude we plot the absolute value of $A_{4c}(r)$ in logarithmic scale in Fig. 9 (b). The linearity in the range of $4 < r < 8$ suggests the presence of an exponential component. However, Eshelby's theory [5, 37] predicts the stress field follows the law of $\frac{1}{r^2}$ in 2D. We interpret this difference between simulation and theory as the evidence of the screening effect on Eshelby's long range field in liquids, similar to the screening effect on Coulomb interaction that leads to an exponential component. We chose a fitting function:

$$|A_{4c}(r)| = \frac{A_c}{r^2}\exp\left(-\frac{r}{\xi}\right), \tag{10}$$

to define the screening length ξ. The fitting result is shown in Fig. 9 (b) by a solid blue line.

We applied the same analysis to the data at other temperatures to determine the temperature dependence of the screening length shown in Fig. 10. It follows a power law with the form of,

$$\xi\left(T^*\right) = \xi_0\left(T^* - T_0\right)^{-\alpha} \tag{11}$$

with $T_0 = 0.48$ and $\alpha = 0.72$. It is interesting that the screening length extrapolates to diverge near the glass transition temperature of $T^* \sim 0.4$, suggesting the role of the stress correlation to play in the glass transition. Unfortunately, the system quickly crystallizes below $T^* = 0.9$ and this divergence could not be confirmed.

4. Eshelby Field

In this section we discuss the Eshelby theory of elastic inclusion [5] to elucidate the stress correlations we observed. When an elastic substance (the 'inclusion') is embedded inside an elastic medium (the 'matrix'), if the shape of the inclusion is different from the hole in the matrix an elastic stress field is generated in and around the inclusion. The resultant elastic fields inside the inclusion and in the matrix can be quantitatively solved through the elegant method devised by Eshelby [5]. It is found that the elastic perturbation to the matrix is long-ranged and anisotropic.

Although the Eshelby's pioneering study on inclusion problems was conducted within the framework of continuum elasticity, it can be applied even to the stresses at the atomic level [38-41]. Moreover, the concept of inclusion effect further extends to disordered materials concerning their plasticity covering from elementary plastic events [6-18] to shear banding [19-21]. In the phenomenological model initiated by Argon and co-workers [15], the local plastic transformations, or equivalently the shear transformation zones noted by Falk and Langer [16, 22], are considered analogous to the Eshelby-type inclusions. From the explicit account of the resultant elastic field accompanying a single plastic event investigated by Picard *et al.* [8], a pattern of $\sim \frac{\cos(4\theta)}{r^2}$ is revealed, presuming the plastic activity occurs at origin in two dimensions. This predicted four-fold symmetry is clearly seen by Nicolas *et al.* [23] in athermal amorphous solids under shear and by Charttoraj and Lemaître [6] in supercooled liquids under shear via spatiotemporal correlation of selected quantities respectively. Whereas these applications successfully elucidated the stress fields in the solid and supercooled states, it has not been applied to the high temperature liquids, although the presence of the stress field in the equilibrium liquid state has been known [39-42]. Even though the Eshelby theory is well-known, we summarize for the sake of clarity the mathematical solutions in 2D in Appendix.

A. Stress distribution

We first illustrate the anisotropic nature of the stress fields induced by a circular inclusion in 2D. In the examples we assume the radius of the inclusion, $a = 0.5$, shear modulus $\mu = 1$, Possion's ratio $\nu = 0.3$, and that the center of the inclusion is placed at origin of the coordinates.

For the case of pure shear transformation strain, *i.e.* $\varepsilon_{12}^{T} = -0.1$ and $\varepsilon_{11}^{T} = \varepsilon_{22}^{T} = 0$, the calculated stress fields are shown in Fig. 11 in the form of two dimensional contour plots. The color scheme is again set to highlight far field. Fig. 11 (a) demonstrates the *x-y* shear stress σ^{s1}, (b) hydrostatic pressure p, and (c) σ^{s2}. The figures clearly show the symmetry of the fields. The shear stress field has eight lobes that amount to two 4θ components, where $\cos(4\theta) < 0$ parts carry positive values while $\cos(4\theta) > 0$ parts assume negative values. It is obvious that the sign of the two components would switch if ε_{12}^{T} turns positive. Moreover, the *x-y* shear stress inside the inclusion is uniform and positive in this specific example. Panels (b) and (c) also manifest evident anisotropicity while the hydrostatic pressure field is rather partitioned into four divisions and σ^{s2} is essentially rotating shear stress field anti-clockwise to the moduli of $\frac{\pi}{8}$.

The Eshelby fields for the case of hydrostatic transformation strains, *i.e.* $\varepsilon_{12}^{T} = 0$ and $\varepsilon_{11}^{T} = \varepsilon_{22}^{T} = -0.1$, are presented in Fig. 12. It is readily recognizable that the panel (a) in Fig. 12 is identical to the panel (b) in Fig. 11. Panels (b) and (c) suggest σ^{xx} and σ^{yy} in the matrix carry the same magnitude yet opposite in sign, and both exhibit the cos (2θ) pattern. Moreover, σ^{s2}

field can be again obtained by rotating σ^{s1} anti-clockwise but to the degree of $\frac{\pi}{4}$. The red disk in the center of panel (b) indicates uniform and positive hydrostatic pressure inside the inclusion.

B. Stress correlation in liquids

The similarity of the patterns in Fig. 3 (Fig. 5 (a)) and in Fig. 11 (a) is obvious, except for the oscillation with r. Also Fig. 5 (b) and Fig. 11 (b), Fig. 5 (c) and Fig. 11 (c) share the same symmetry. The same applies to Fig. 6 and Fig. 12. Thus clearly the angular dependence of the stress correlations in the liquid state is explained in terms of the Eshelby's inclusion model. The oscillation with *r* is related to the PDF and the discrete nature of the atomic structure. In the case of the *x-y* shear stress autocorrelation it is related the derivative of the PDF as shown in Figs. 7. For the cases of others the oscillation is directly related to the pair correlation function as shown in Fig. 8.

5. Conclusions

A liquid behaves like a solid at a short timescale. Therefore it can support the elastic stress field for a short time. This results in the stress correlations in the liquids, which contribute to the viscosity. So far, however, only the isotropic stress correlations have been studied. In this article we extended our research into the anisotropic stress correlations. We found that the spatial correlations of the atomic level stresses share the same symmetry with the stress fields in the matrix in the Eshelby's inclusion model. Specifically, the *x-y* shear stress autocorrelation function exhibits the familiar four-fold symmetry, the correlation of hydrostatic pressure of one particle and *x-y* shear stress of the others characterizes a $\cos(2\theta)$ symmetry, and so forth. In our view, these long-range anisotropic correlation functions indicate the existence of the Eshelby-type inclusion effect in the simulated 2D Yukawa liquids. In the Eshelby model the stress field is generated by the mismatch in shape between the inclusion and the hole in the matrix. In the present case the atomic-level stress is caused by the mismatch between the shape of the atom (spherical) and the hole in the nearest neighbor shell. The shear stress is generated when the nearest neighbor shell has an elliptic distortion, and the pressure occurs when the size of the atom and that of the nearest neighbor hole are not the same [39-41, 43, 44].

However, we found that the amplitude of anisotropic component of x-y shear stress autocorrelation function does not follow Eshelby's prediction of $\frac{1}{r^2}$ but has additional exponential decay with distance. This difference can be perceived as screening effect that has temperature dependence. The relevant screening length appears to follow a power law, diverging at a temperature close to the glass transition temperature, suggesting a possible role for the stress correlation to play in the glass transition phenomenon. This issue, however, requires further study in the supercooled temperature range.

It is also of interest to see if the strong stress correlations seen here in 2D are also present in 3D. We have collected some preliminary results on 2D and 3D liquids interacting via modified Johnson potential [45], and similar results are obtained. However, more detailed studies are required to answer this question more definitively.

Acknowledgments

The authors thank J. S. Langer, J. R. Morris and J. Bellissard for useful discussions. This research has been supported by the Department of Energy, Office of Sciences, Basic Energy Sciences, Materials Science and Engineering Division.

Appendix: Mathematical solutions of the Eshelby problem in 2D

Here we discuss two distinct methods of solving the two-dimensional circular inclusion problems. The simplest cases of homogeneous, isotropic and infinite matrix embedding an inclusion that shares the same elastic moduli are considered here. Furthermore, there is neither external loading nor body force. Hence the elastic field inside the inclusion and matrix is exclusively determined by the transformation strain of the inclusion ε^T and consequent elastic responses.

The first method can be deemed as the special cases of Eshelby's [5] original approach in three dimensions under plane strain condition. In this condition, the inclusion has a cylindrical shape with its axis of symmetry lying along the z axis and being infinitely long. In addition, if the components of transformation strains that are related to the z direction, *i.e.* ε_{xz}^T, ε_{yz}^T, and ε_{zz}^T, are zero, then the elastic condition on the cross sectional plane is equivalent to the desired two dimensional counterpart. In practice, a prolate spheroidal inclusion with its polar axis extending over several orders of magnitude larger than the equatorial diameter is already a reasonable approximation of plane strain condition. Therefore, the strain field on the short semi-axis plane can be acquired from derivatives of displacements through numerical integration either using Eq. (A1) or Eq. (A2). With the advent of powerful computational resources and sophisticated numerical calculations recipes, such as finite element method, these integrations are no longer formidable tasks.

$$\begin{aligned} u_{i,m}(\vec{r}) = -\frac{1}{16\pi\mu(1-\nu)}\int dS(\overrightarrow{r'})\frac{n_k}{\left|\vec{r}-\overrightarrow{r'}\right|^3}\sigma^T_{kj}\Big\{&4(1-\nu)(x_m-x'_m)\delta_{ij}-(x_j-x'_j)\delta_{im}-(x_i-x'_i)\delta_{jm} \\ &-(x_m-x'_m)\delta_{ij}+3\frac{1}{\left|\vec{r}-\overrightarrow{r'}\right|^2}(x_m-x'_m)(x_i-x'_i)(x_j-x'_j)\Big\}, \end{aligned} \tag{A1}$$

$$\begin{aligned} u_{i,m}(\vec{r}) = \frac{1}{16\pi\mu(1-\nu)}\int dV(\overrightarrow{r'})\frac{\sigma^T_{kj}}{\left|\vec{r}-\overrightarrow{r'}\right|^3}\Big\{&(1-2\nu)\left[(\delta_{mk}-3l_kl_m)\delta_{ij}+(\delta_{mj}-3l_ml_j)\delta_{ik}\right] \\ &-(\delta_{mi}-3l_ml_i)\delta_{jk}+3\left[l_jl_k\delta_{im}+l_il_k\delta_{jm}+l_il_j\delta_{km}-5l_il_jl_kl_m\right]\Big\}. \end{aligned} \tag{A2}$$

Eq. (A1) integrates over the surface of the inclusion, which is assembly of $\overrightarrow{r'}$. Indices in subscripts denote any one of three Cartesian components, δ Kronecker delta function, μ shear modulus, υ Poisson's ratio, σ^T stress calculated from transformation strain elastically via Hook's law, and $\vec{n}$ unit normal vector of surface element $dS(\overrightarrow{r'})$. With employment of Einstein's notation, the repeated indices suggest summation, *e.g.* $x_ix_i = x_1x_1 + x_2x_2 + x_3x_3$, and an index preceded by a comma requires derivative operation on the specified direction, *e.g.* $u_{i,m} = \frac{\partial u_i}{\partial x_m}$. Applying Gauss's theorem to Eq. (A1) gives rise to Eq. (A2) that integrates over volume of the inclusion. l represents the unit vector starting from volume element $dV(\overrightarrow{r'})$ to the point of interest $\vec{r}$.

Comparing to degenerating solutions derived in three dimensions into 2D version, complex variable formalism is generally more favorable for the plane theory of elasticity. Details concerning this method can be found from Refs. [46] and [47]. In this formalism, each point on the plane is represented by $x = x_1 + ix_2$, where $i^2 = -1$, and the corresponding elastic field can be completely mapped out via two bi-harmonic functions of x, *e.g.* $\phi(x)$ and $\psi(x)$, through the following relationships:

$$\sigma_{11}(x) + \sigma_{22}(x) = 4Re\{\phi'(x)\}, \tag{A3}$$

$$\sigma_{22}(x) - \sigma_{11}(x) + 2i\sigma_{12}(x) = 2\{\bar{x}\phi''(x) + \psi''(x)\}, \tag{A4}$$

$$2\mu(u_1 + iu_2) = \kappa\phi(x) - x\overline{\phi'(x)} - \overline{\psi'(x)}, \tag{A5}$$

where a prime corresponds to differential operation with respect to x while double primes mean two times of such procedures. Moreover, a bar implies complex conjugate operation, Re indicates taking real part of the object, and κ equals either $3 - 4\upsilon$ under plane strain condition or $\frac{3-\upsilon}{1+\upsilon}$ in the condition of plane stress.

Within this framework, Jaswon and Bhargava [37] unraveled Eshelby's inclusion problems in two dimensions. The solutions were given separately for an elliptic inclusion suffering from either pure principal or shear transformation strains. In the event of a circular inclusion, the refined $\phi(x)$ and $\psi'(x)$ valid for matrix are presented below.

For principal pressure condition, *i.e.* $\varepsilon_{12}^T = 0$,:

$$\phi(x) = \frac{\mu a^2}{(\kappa+1)x}(\varepsilon_{11}^T - \varepsilon_{22}^T), \tag{A6}$$

$$\psi'(x) = -\frac{2\mu a^2}{(\kappa+1)x}(\varepsilon_{11}^T + \varepsilon_{22}^T) + \frac{\mu a^4}{(\kappa+1)x^3}(\varepsilon_{11}^T - \varepsilon_{22}^T). \tag{A7}$$

For shear stress condition, *i.e.* $\varepsilon_{11}^T = \varepsilon_{22}^T = 0$,:

$$\phi(x) = i\frac{2\mu a^2}{(\kappa+1)x}\varepsilon_{12}^T, \tag{A8}$$

$$\psi'(x) = i\frac{2\mu a^4}{(\kappa+1)x^3}\varepsilon_{12}^T, \tag{A9}$$

where a is the radius of the inclusion.

References:

1. J.-P. Hansen and I. R. McDonald, *Theory of Simple Liquids* (Academic Press, Amsterdam, 2006) 3rd ed.
2. T. Egami, K. Maeda and V. Vitek, Phil. Mag. A **41**, 883 (1980).
3. V. A. Levashov, J. R. Morris and T. Egami, Phys. Rev. Lett. **106,** 115703 (2011).
4. M. P. Allen and D. J. Tildesley, *Computer Simulation of Liquids* (Oxford University Press, New York, 1987).
5. J. D. Eshelby, Proc. Roy. Soc. London, Ser. A **241**, 376 (1957).
6. J. Chattoraj and A. Lemaître, Phys. Rev. Lett. **111**, 066001 (2013).
7. F. Puosi, J. Rottler, and J.-L. Barrat, Phys. Rev. E **89**, 042302 (2014).
8. G. Picard, A. Ajdari, F. Lequeux, and L. Bocquet, Eur. Phys. J. E. **15**, 371 (2004).
9. C. E. Maloney and A. Lemaître, Phys. Rev. E **74**, 016118 (2006).
10. A. Tanguy, F. Léonforte, J. L. Barrat, Eur. Phys. J. E **20**, 355 (2006).
11. A. Lemaître and C. Caroli, Phys. Rev. E **76**, 036104 (2007).
12. M. Tsamados, A. Tanguy, F. Léonforte, and J.-L. Barret, Eur. Phys. J. E **26**, 283 (2008).
13. A. Lemaître and C. Caroli, Phys. Rev. Lett. **103**, 065501(2009).
14. A. Le Bouil, A. Amon, S. McNamara, and J. Crassous, Phys. Rev. Lett. **112**, 246001 (2014).
15. V. V. Bulatov and A. S. Argon, Modell. Simul. Mater. Sci. Eng. **2**, 167 (1994).
16. J. S. Langer, Phys. Rev. E **64**, 011504 (2001).
17. C. Maloney and A. Lemaître, Phys. Rev. Lett. **93**, 016001 (2004).
18. P. Cao, H. S. Park, and X. Lin, Phys. Rev. E **88**, 042404 (2013).
19. R. Dasgupta, H. G. E. Hentschel, and I. Procaccia, Phys. Rev. E **87**, 022810 (2013).
20. R. Dasgupta, H. G. E. Hentschel, and I. Procaccia, Phys. Rev. Lett. **109**, 255502 (2012).
21. K. Martens, L. Bocquet, and J.-L. Barrat, Soft Matter **8**, 4197 (2012).
22. M. L. Falk and J. S. Langer, Phys. Rev. E **57**, 7192 (1998).
23. A. Nicolas, J. Rottler, and J.-L. Barrat, Eur. Phys. J. E. **37**, 50 (2014).
24. P. Schall, D. A. Weitz, and F. Spaepen, Science **318**, 1895 (2007).
25. K. E. Jensen, D. A. Weitz and F. Spaepen, Phys. Rev. E **90,** 042305 (2014).
26. S. Plimpton, J. Comp. Phys. **117**, 1 (1995).
27. W. K. Qi, S. M. Qin, X. Y. Zhao, and Y. Chen, J. Phys.: Condens. Matter **20**, 245102 (2008).
28. W. K. Qi, Z. Wang, Y. Han, and Y. Chen, J. Chem. Phys. **133**, 234508 (2010).
29. H. Yukawa, Proc. Phys. Math. Soc. Jpn. **17**, 48 (1935).
30. W.-R. Chen, L. Porcar, Y. Liu, P. D. Butler, and L. J. Magid, Macromolecules, **40**, 5887 (2007)
31. S. Z. Lin, B. Zheng, and S. Trimper, Phys. Rev. E **73**, 066106 (2006).
32. B. I. Halperin and D. R. Nelson, Phys. Rev. Lett. **41**, 121 (1978).
33. J. M. Kosterlitz and D. J. Thouless, J. Phys. C **6**, 1181 (1973).
34. D. R. Nelson and B. I. Halperin, Phys. Rev. B **19**, 2457 (1979).
35. A. P. Young, Phys. Rev. B **19**, 1855 (1979).
36. S. T. Chui, Phys. Rev. Lett. **48**, 933 (1982).
37. M. A. Jaswon and R. D. Bhargava, Math. Proc. Cambridge **57**, 669 (1961).
38. T. L. Hoang, A. Arsenlis, H. J. Lee-Voigt, D. C. Chrzan, and B. D. Wirth, Model. Simul. Mater. Sci. Eng. **19**, 085001 (2011).

39. T. Egami and D. Srolovitz, J. Phys. F: Metal Phys. **12**, 2141 (1982).
40. T. Egami, S. J. Poon, Z. Zhang and V. Keppens, Phys. Rev. B **76,** 024203 (2007).
41. T. Egami, Progr. Mater. Sci. **56,** 637 (2011).
42. V. A. Levashov, J. R. Morris, and T. Egami, J. Chem. Phys. **138**, 044507 (2013).
43. T. Egami and S. Aur, J. Non-Cryst. Solids **89**, 60 (1987).
44. V. A. Levashov, T. Egami, R. S. Aga, and J. R. Morris, Phys. Rev. B **78**, 064205 (2008).
45. V. A. Levashov, T. Egami, R. S. Aga, and J. R. Morris, Phys. Rev. E **78**, 041202 (2008).
46. N. I. Muskhelishvili, *Some Basic Problems of the Mathematical Elasticity Theory* (Noordhoff, Leyden, 1977) 4th ed.
47. I. S. Sokolnikoff, *Mathematical Theory of Elasticity* (McGraw-Hill, New York, 1956) 2nd ed.

Figure captions:

Figure 1. Potential energy per atom as a function of reduced temperature. The divergence from linearity at temperature around 0.9 suggests onset of melting process while its recurrence around 1.0 indicates entrance to liquid phase.

Figure 2. (Color online) Spatial correlation function of bond orientational order parameter at $T^* = 0.9$ (top black line), $T^* = 0.95$ (upper middle green line), $T^* = 1.0$ (lower middle pink line) and $T^* = 1.1$ (bottom dark red line). $g_6(r)$ converges to a finite value only at crystalline phase while it decays algebraically at hexatic phase and exponentially at liquid phase. Hence the phase behavior at each presented temperature is readily identified.

Figure 3. (Color) The spatial shear stress correlation function computed at $T^* = 1$. In panel (a), the scale of color scheme matches the intensity of correlation function while in panel (b) the scale is set to highlight remote area.

Figure 4. (Color) Pair distribution function with angular dependence for crystalline phase (a) and liquid phase (b). In crystalline phase, each particle has exactly six nearest neighbors and long range positional order is readily recognized while liquid phase has isotropic packing of particles.

Figure 5. (Color) The spatial correlation of x-y shear stress and x-y shear stress (a), hydrostatic pressure (b) and σ^{s2} (c) calculated for liquid phase at $T^* = 1$.

Figure 6. (Color) The spatial correlation of hydrostatic pressure and *x*-*y* shear stress (a), hydrostatic pressure (b), and σ^{s2} (c) computed at $T^* = 1$.

Figure 7. (Color online) The comparison of spatial *x*-*y* shear stress autocorrelation in the 0° direction (a) and 45° direction (b) against the derivative of pair distribution function. The amplitudes of the highest peaks are rescaled to unities.

Figure 8. (Color online) The comparison between oscillations of $C_{p,p}(\vec{r})$ (panel (a)), $C_{p,s1}(\vec{r})$ (panel (b)), $C_{p,s2}(\vec{r})$ (panel (c)), and $C_{s1,s2}(\vec{r})$ (panel (d)) along respective maximum intensity directions and that of pair correlation function, $h(r)$. The correlation functions are rescaled to share the same amplitude with pair correlation function at the third peak position of the latter, *i.e.* $r = 2.68$.

Figure 9. (Color online) The cos(4*θ*) component of spatial *x*-*y* shear stress autocorrelation function computed at $T^* = 1$. Panel (a) presents result in linear scale and panel (b) shows its absolute value in logarithmic scale along with a fitting curve.

Figure 10. (Color online) Temperature dependence of screening length extracted from cos(4*θ*) component of *x*-*y* shear stress autocorrelation function (black solid circle) and a power law fitting curve (blue solid line).

Figure 11. (Color) 2D contour plot of *x*-*y* shear stress σ^{s1} (a), hydrostatic pressure p (b), and σ^{s2} (c) created by a circular inclusion undergoing shear transformation strain.

Figure 12. (Color) The stress fields induced by a circular inclusion suffering from principal transformation strain. The arrangement of panels is identical to that of Fig. 11.

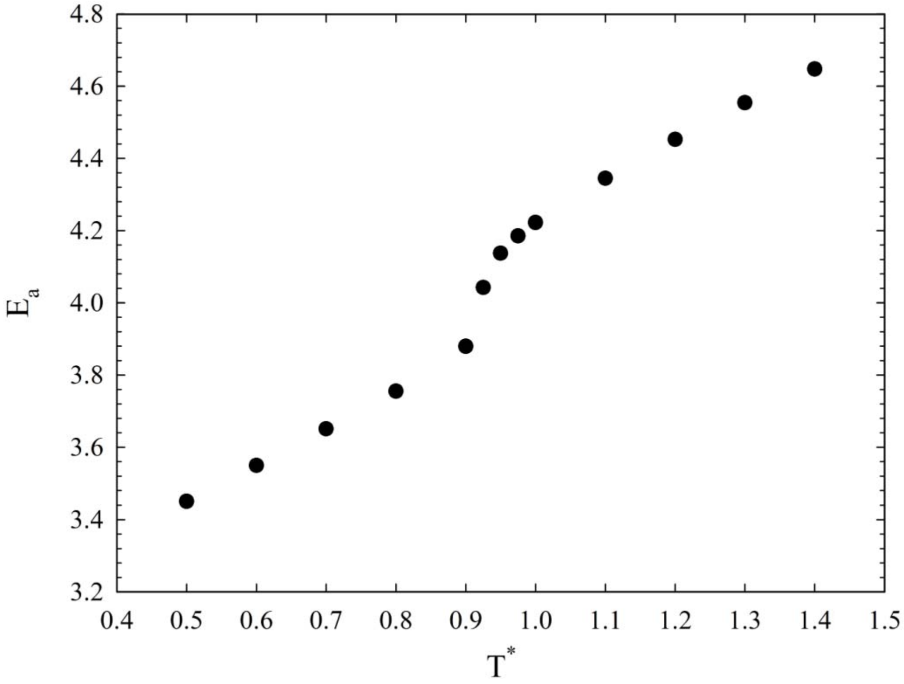

4.8
4.6
4.4
4.2
4.0
3.8
3.6
3.4
3.2
E_a
0.4
0.5
0.6
0.7
0.8
0.9
1.0
1.1
1.2
1.3
1.4
1.5
T^*

Fig. 1

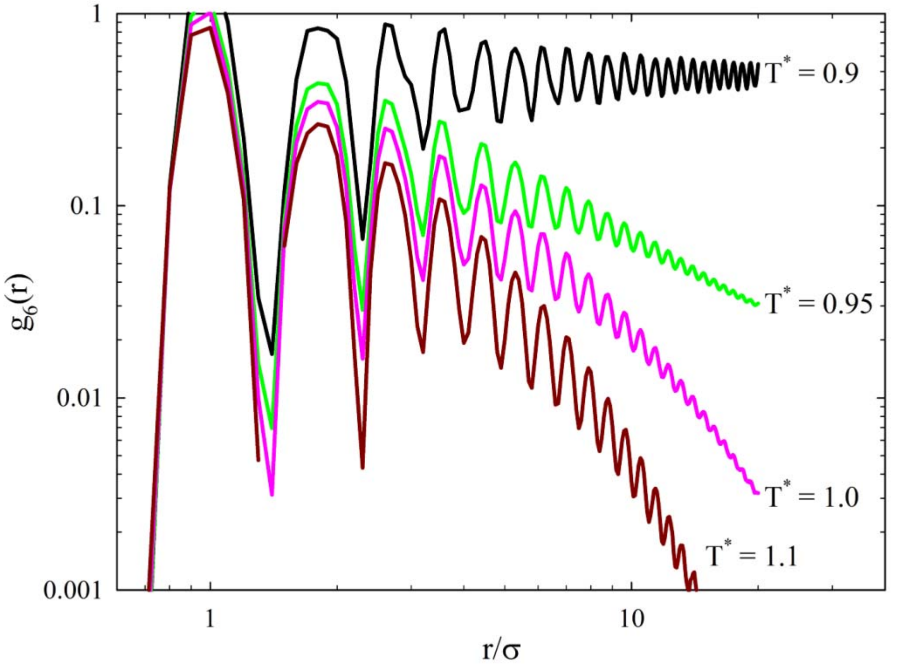

1
0.1
0.01
0.001
$g_6(r)$
1
10
r/σ
$T^* = 0.9$
$T^* = 0.95$
$T^* = 1.0$
$T^* = 1.1$

Fig. 2

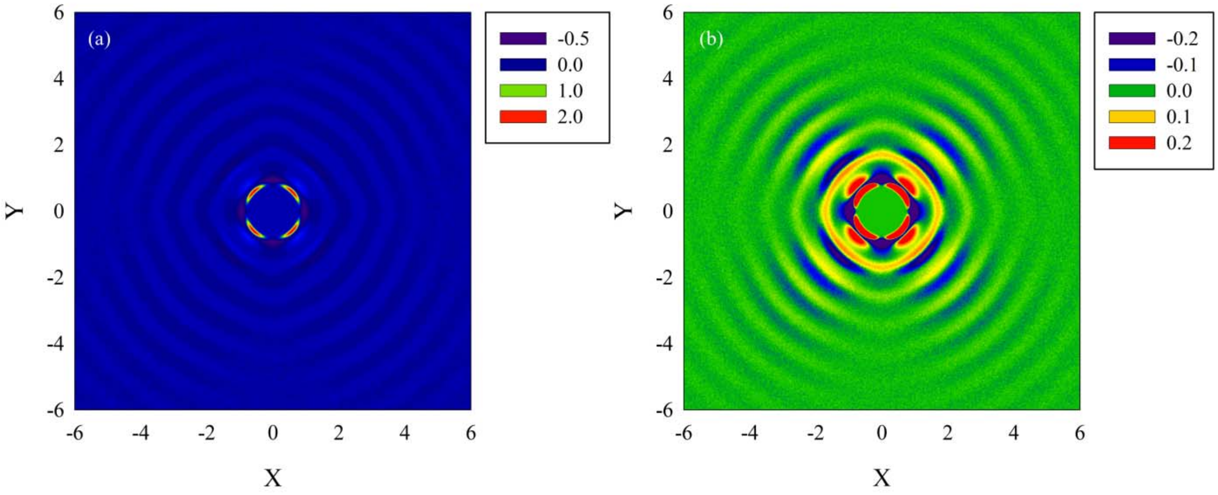

Fig. 3

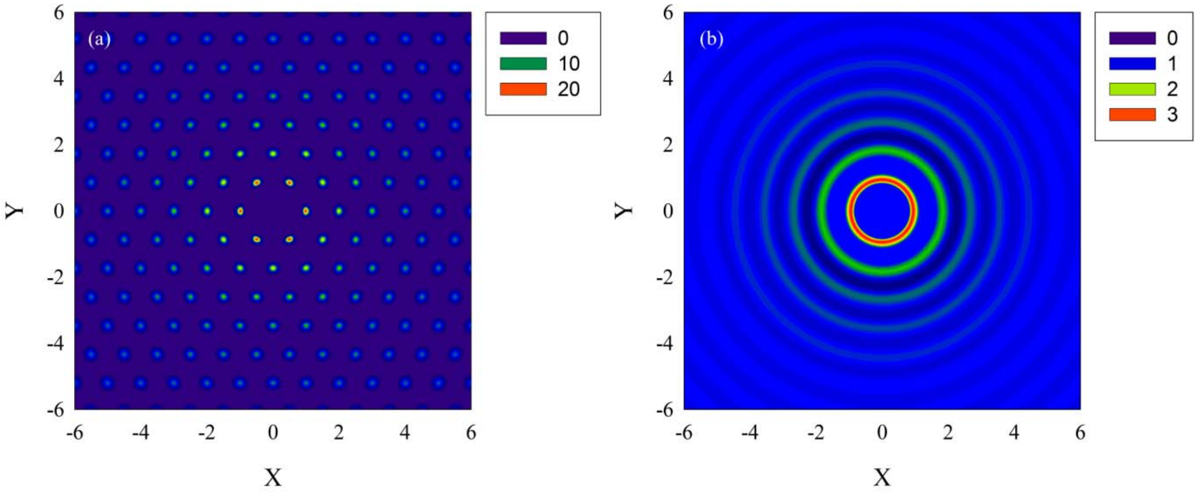

Fig. 4

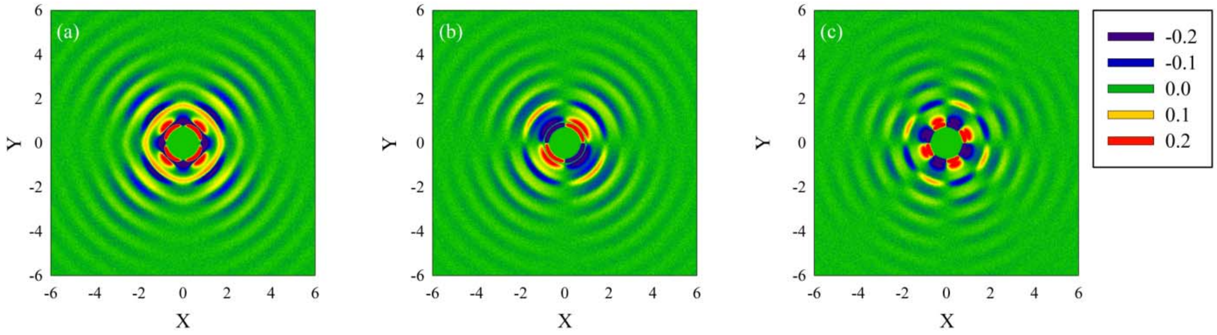

Fig. 5

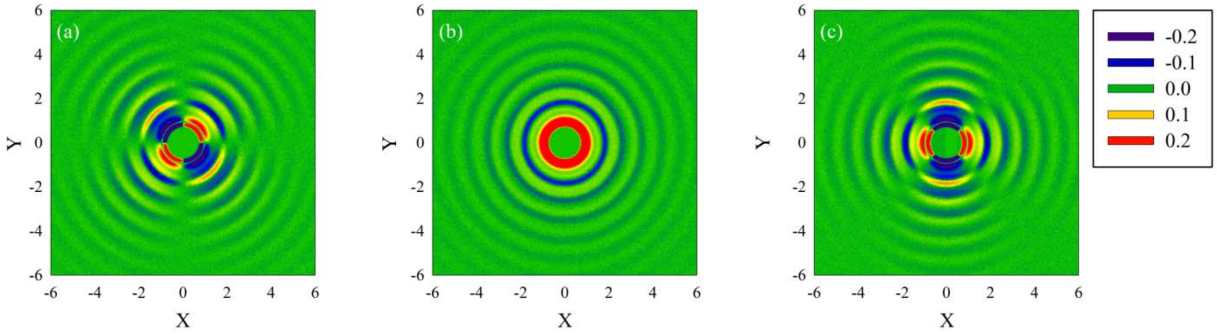

Fig. 6

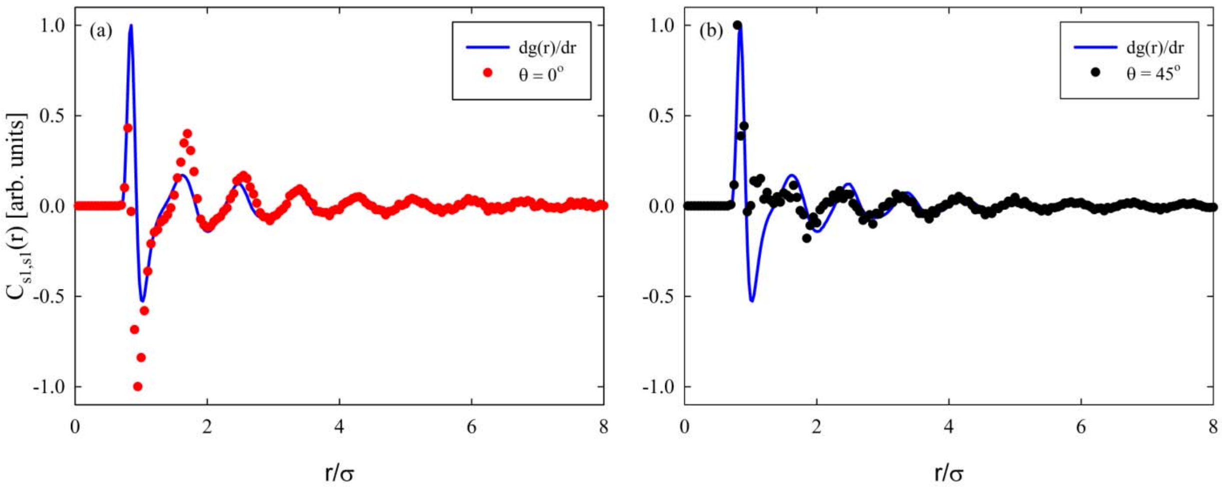

Fig. 7

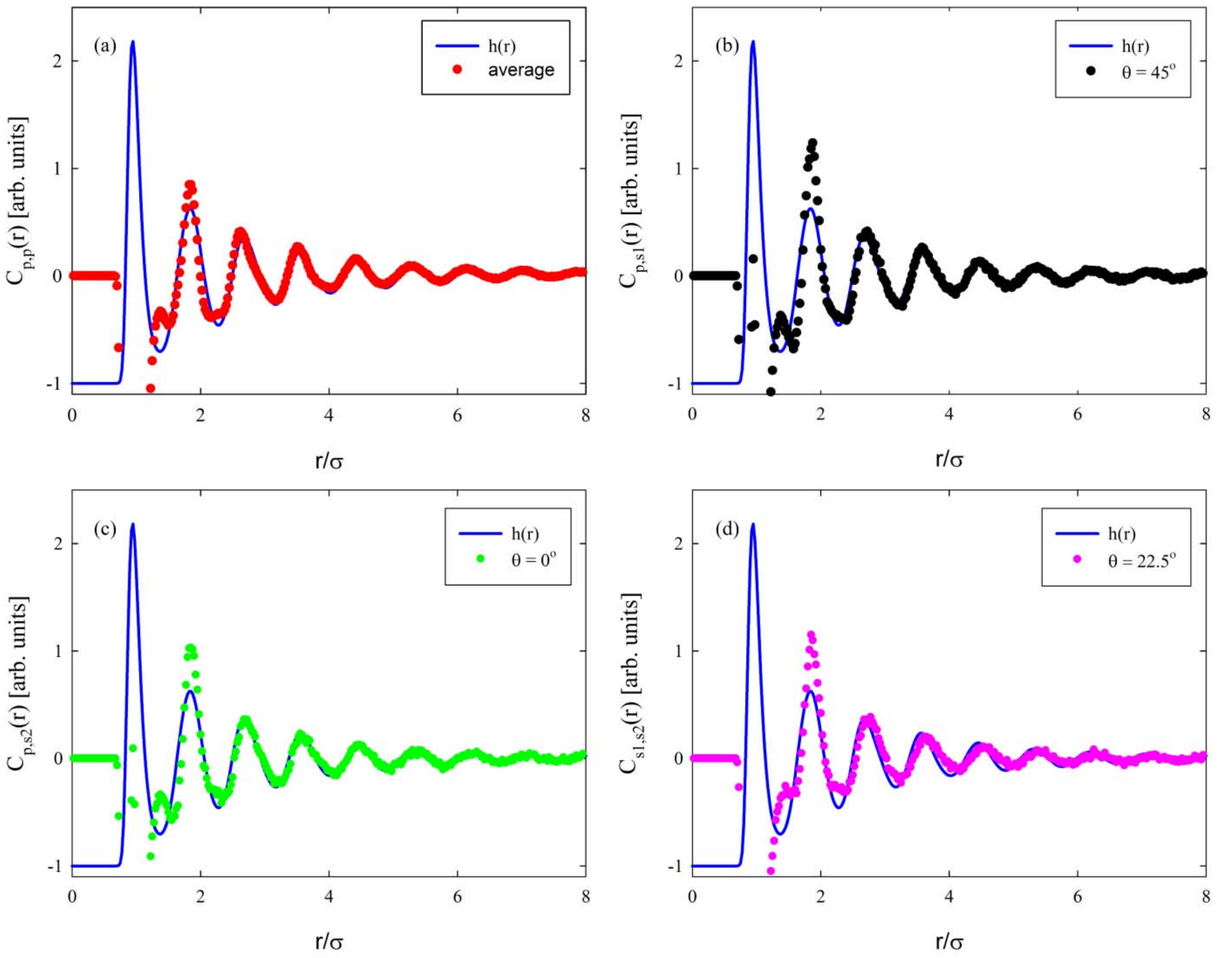
(a)
h(r)
average
$C_{p,p}(r)$ [arb. units]
(b)
h(r)
$\theta = 45^o$
$C_{p,s1}(r)$ [arb. units]
(c)
h(r)
$\theta = 0^o$
$C_{p,s2}(r)$ [arb. units]
(d)
h(r)
$\theta = 22.5^o$
$C_{s1,s2}(r)$ [arb. units]
r/σ
0
2
4
6
8
-1
0
1
2

Fig. 8

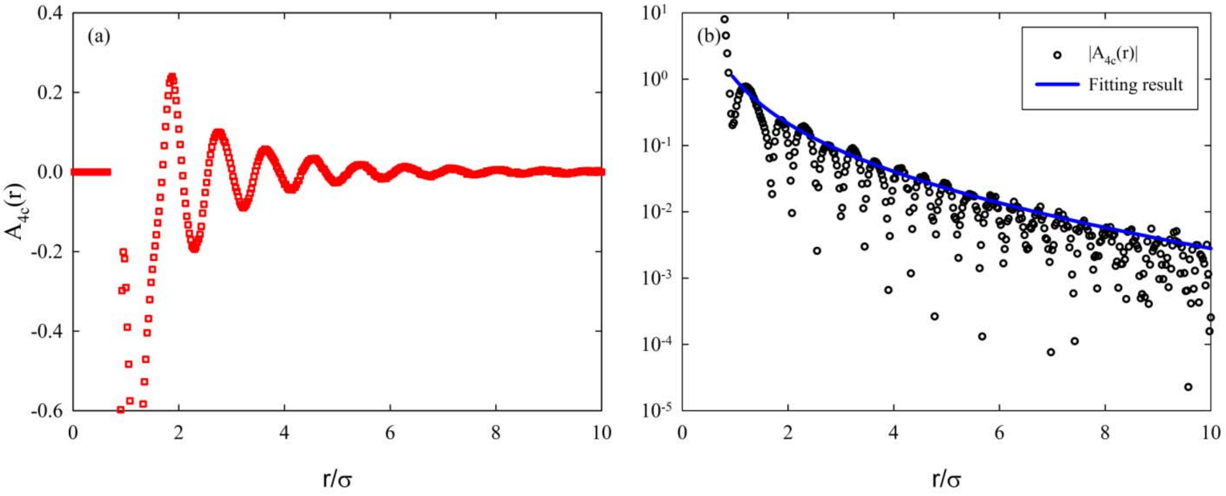
(a)
$A_{4c}(r)$
0.4
0.2
0.0
-0.2
-0.4
-0.6
0
2
4
6
8
10
r/σ
(b)
$|A_{4c}(r)|$
Fitting result
10^{1}
10^{0}
10^{-1}
10^{-2}
10^{-3}
10^{-4}
10^{-5}
0
2
4
6
8
10
r/σ

Fig. 9

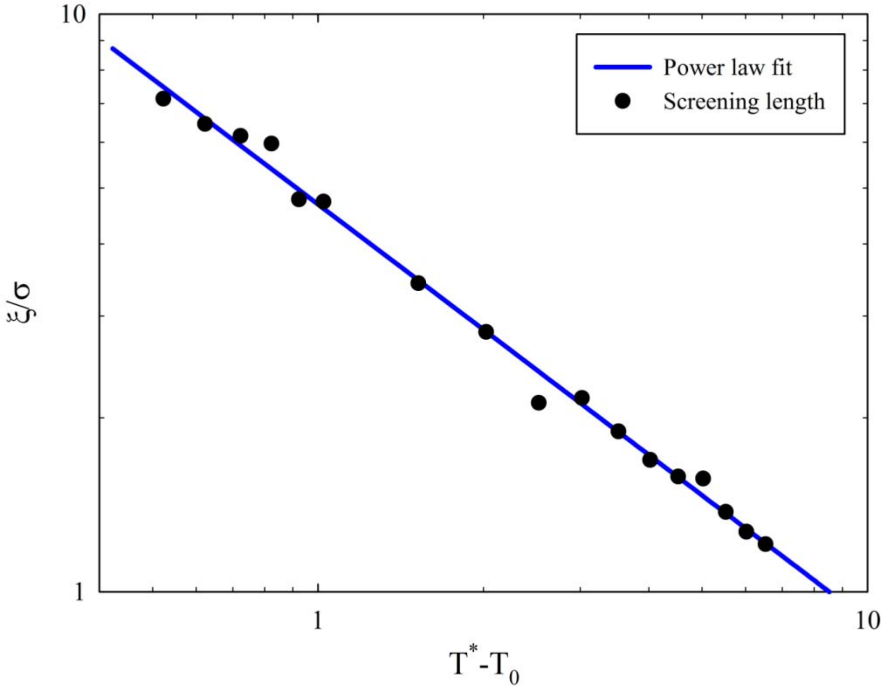
Power law fit
Screening length
ξ/σ
10
1
1
10
$T^{*}-T_{0}$

Fig. 10

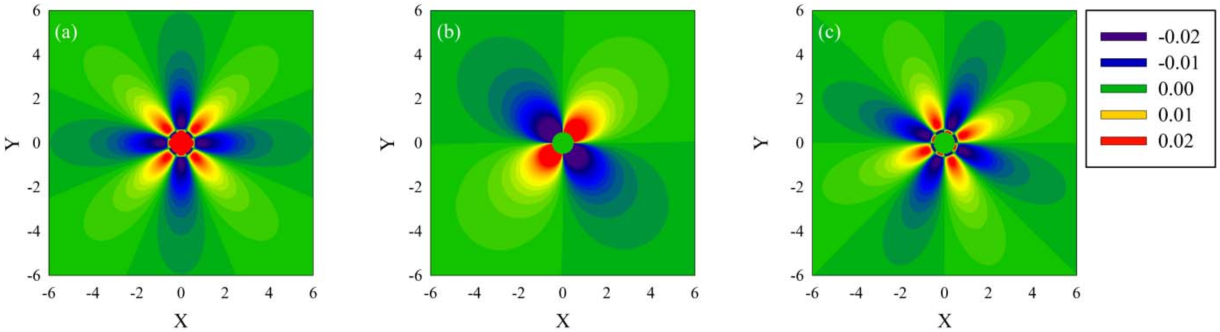
(a)
(b)
(c)
Y
X
6
4
2
0
-2
-4
-6
-0.02
-0.01
0.00
0.01
0.02

Fig. 11

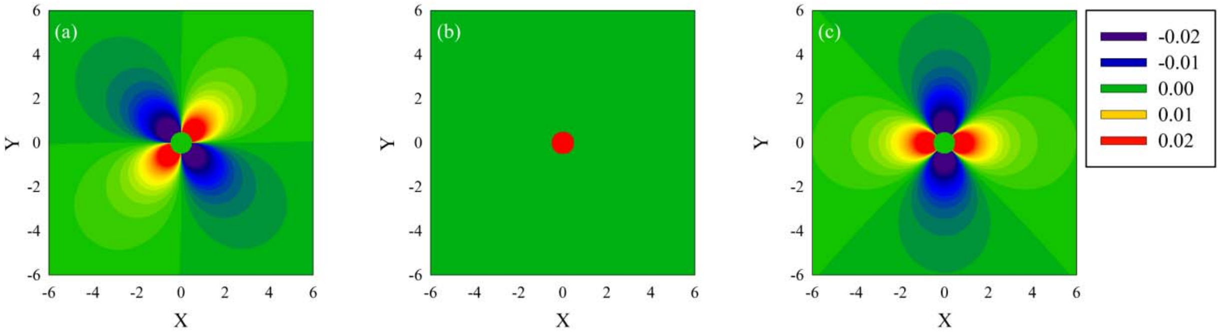
(a)
(b)
(c)
Y
X
6
4
2
0
-2
-4
-6
-0.02
-0.01
0.00
0.01
0.02

Fig. 12